

Full length article

Radiation-induced segregation on defect clusters in single-phase concentrated solid-solution alloys



Chenyang Lu ^a, Taini Yang ^a, Ke Jin ^b, Ning Gao ^c, Pengyuan Xiu ^a, Yanwen Zhang ^{b,d},
Fei Gao ^a, Hongbin Bei ^b, William J. Weber ^{d,b}, Kai Sun ^e, Yan Dong ^e, Lumin Wang ^{a,e,*}

^a Department of Nuclear Engineering and Radiological Sciences, University of Michigan, Ann Arbor, MI, 48109, USA

^b Materials Science and Technology Division, Oak Ridge National Laboratory, Oak Ridge, TN, 37831, USA

^c Institute of Modern Physics, Chinese Academy of Sciences, Lan Zhou, Gansu, 73000, China

^d Department of Materials Science and Engineering, University of Tennessee, Knoxville, TN, 37996, USA

^e Department of Materials Science and Engineering, University of Michigan, Ann Arbor, MI, 48109, USA

ARTICLE INFO

Article history:

Received 12 September 2016

Received in revised form

12 December 2016

Accepted 9 January 2017

Available online 12 January 2017

Keywords:

Radiation induced segregation

Single-phase concentrated solid-solution alloys

High-entropy alloys

Electron energy loss spectroscopy

Molecular static simulations

ABSTRACT

A group of single-phase concentrated solid-solution alloys (SP-CSAs), including NiFe, NiCoFe, NiCoFeCr, as well as a high entropy alloy NiCoFeCrMn, was irradiated with 3 MeV Ni²⁺ ions at 773 K to a fluence of 5×10^{16} ions/cm² for the study of radiation response with increasing compositional complexity. Advanced transmission electron microscopy (TEM) with electron energy loss spectroscopy (EELS) was used to characterize the dislocation loop distribution and radiation-induced segregation (RIS) on defect clusters in the SP-CSAs. The results show that a higher fraction of faulted loops exists in the more compositionally complex alloys, which indicate that increasing compositional complexity can extend the incubation period and delay loop growth. The RIS behaviors of each element in the SP-CSAs were observed as follows: Ni and Co tend to enrich, but Cr, Fe and Mn prefer to deplete near the defect clusters. RIS level can be significantly suppressed by increasing compositional complexity due to the sluggish atom diffusion. According to molecular static (MS) simulations, “disk” like segregations may form near the faulted dislocation loops in the SP-CSAs. Segregated elements tend to distribute around the whole faulted loop as a disk rather than only around the edge of the loop.

© 2017 The Author(s). Published by Elsevier Ltd. This is an open access article under the CC BY-NC-ND 4.0 license (<http://creativecommons.org/licenses/by-nc-nd/4.0/>).

1. Introduction

Recently, a novel class of materials called single-phase concentrated solid-solution alloys (SP-CSAs), including high entropy alloys (HEAs), has drawn much attention. Unlike traditional alloys, SP-CSAs contain two or more principle elements in equal or near-equal molar ratios. These elements form random solid solutions in simple face-centered cubic (fcc) or body-centered cubic (bcc) lattice structures, which grant SP-CSAs extraordinary properties, such as high yield strength, high thermal stability and hardness, high-temperature strength, great wear and fatigue resistance, and excellent corrosion resistance [1–4]. Notably, SP-CSAs also exhibit promising radiation resistance as demonstrated by theoretical and experimental studies [5–9]. Because of these superior properties,

SP-CSAs are considered as potential candidates for fission and fusion reactor applications.

High-level lattice distortion and compositional complexity in SP-CSAs could change the process of energy dissipation and facilitate the recovery of radiation damage in the very early stages of irradiation [5,6,8,10]. Zhang et al. found that chemical disorder effectively reduced the electron mean free path, electrical and thermal conductivities, which significantly delayed defect evolution during ion irradiation at room temperature [5]. Jin et al. found that equiatomic NiFe presented significant delay in damage accumulation and evolution compared to pure nickel and NiCo at room temperature [11]. Using cross-sectional transmission electron microscopy (TEM), Lu et al. demonstrated that defect clusters migrated slower in NiFe than in pure nickel and NiCo at room temperature [6]. This finding was confirmed by the molecular dynamics (MD) simulations from Aidhy et al. [10]. Similar performance persists even at elevated temperatures and at higher irradiation doses. Kumar et al. found that non-single phase FeNiMnCr exhibited good microstructural stability and mechanical

* Corresponding author. Department of Nuclear Engineering and Radiological Sciences, University of Michigan, Ann Arbor, MI, 48109, USA.

E-mail address: lmwang@umich.edu (L. Wang).

behavior under high temperature irradiation up to 10 displacement per atom (dpa) [9]. Jin et al. reported that HEA alloy NiCoFeCrMn showed much higher swelling tolerance than pure nickel when irradiated by 3 MeV Ni ions to a peak dose of 60 dpa at 773 K [7]. Lu et al. performed detailed studies on a group of SP-CSAs (from binary to quinary alloys) irradiated to high doses by cross-sectional TEM characterization. They observed a unique void and dislocation loop separation, successfully linking the distribution with the defect cluster migration behavior, and explained the intrinsic mechanisms of void resistance in SP-CSAs [12]. In spite of these efforts, further study is required to examine the evolution of dislocation loops and local chemical segregation, particularly as a function of the chemical composition.

Radiation-induced segregation (RIS) is a typical radiation-induced phenomenon caused by the preferential interaction between the flux of vacancy and interstitial point defects and the flux of solutes to point defect sinks [13], such as grain boundaries, dislocations and voids. RIS could result in serious degradation of mechanical properties of structural materials, such as radiation-induced hardening and embrittlement. Currently, most studies focus on the RIS behavior of grain boundaries. For instance, radiation-induced depletion of Cr at grain boundaries was observed in austenitic stainless steels for decades, and it was widely known as one of the contributing factors to irradiation-assisted stress corrosion cracking (IASCC) [14–16]. Kumar et al. claimed that FeNiMnCr HEA exhibited better resistance against RIS on grain boundaries compared to conventional Fe-20Cr-24Ni alloy [9]. On the other hand, few studies on RIS to the defect clusters have been reported. The small scale of defect clusters and low magnitude of RIS around them make the characterization very difficult. Nevertheless, such studies are important because RIS around defect clusters may alter the defect cluster evolution under continued irradiation and thus affect the mechanical properties of the material. For example, the austenite structure can be destabilized due to the depletion of Ni in the matrix while Ni atoms segregate to the void/dislocation and/or loop/grain boundaries caused by RIS [17]. Jiao [14] and Dong [18] observed RIS on dislocation loops in austenitic stainless steels using atom probe tomography (APT); however, the exact nature and structure of the loops could not be identified by APT. Another interesting and open question is what are the configurations of the segregated atoms near the loop. Do they form a ring around the edge of the loop, or a “disk-like” plate within the whole loop? APT results from Jiao [7] and Dong [18] indicate that the segregation is more like first scenario, but it is questionable whether the segregation regions of both perfect and faulted dislocation loops are the same.

In this study, conventional TEM characterization was applied in two-beam condition to compare the dislocation loop distribution in Ni and a group of Ni-containing SP-CSAs after high temperature ion irradiation. The mechanisms of irradiation-induced hardening in SP-CSAs can be correlated with a previous study [7]. RIS on defect clusters (loops and voids) was observed and analyzed by ultra-fast electron energy loss spectroscopy (EELS) system equipped on a Cs-corrected scanning TEM (STEM). Molecular static (MS) simulation has also been conducted to clarify the shape of the segregation region and reveal the intrinsic segregation mechanism.

2. Experiments

2.1. Alloys

Pure Ni, Co, Fe, Cr and Mn elemental metals (>99.9% pure) were used to prepare the alloy ingots by arc-melting. Detailed information of alloy preparation was described in a previous study [7]. Four Ni-containing single-phase fcc equiatomic alloys, single crystal

binary NiFe, ternary NiCoFe, and quaternary NiCoFeCr as well as a polycrystalline quinary alloy NiCoFeCrMn (with millimeter size grains) were prepared. Prior to irradiation, the specimens were ground using up to #4000 grit SiC paper, followed by chemical-mechanical polishing with up to 0.05 μm colloidal silica polishing solutions. “Mirror-like” surfaces were achieved with roughness below 3 nm.

2.2. Ion irradiation

The specimens were irradiated with 3 MeV Ni^{2+} ions to a fluence of 5×10^{16} ions/ cm^2 at 773 K in the Ion Beam Materials Laboratory (IBML) at the University of Tennessee. The flux was controlled at 2.8×10^{12} / cm^2s . A rastered beam was employed to ensure homogeneous irradiation. Ion irradiation doses and stopping range in samples were computed by SRIM 2013 assuming a displacement threshold energy of 40 eV in Kinchin-Pease option [19]. The damage and implanted ion concentration profiles are shown in Fig. 1. The region of 500 ± 100 nm with a dose about 38 ± 5 dpa was chosen for the statistic of loop distribution and chemical characterization, in order to avoid the artificial effects associated with the surface sinks and the injected interstitial effects. The studied region is highlighted as shown in Fig. 1. To be noted, the loop images shown in Fig. 2 are from a larger region for enhancing visualization and a better comparison.

2.3. Microstructural characterization, EELS data acquisition and analysis

Cross-sectional TEM foils from irradiated samples were all prepared by focused ion beam (FIB) lift-out techniques using a FEI Helios Nanolab Dualbeam workstation. In order to remove unwanted FIB-induced damage, which would confuse the observation of small defect clusters created by Ni ions, “Flash polishing” was subsequently conducted. Significant improvement of the TEM sample quality after “flash polishing” was presented in Ref. [6]. Prior to characterization, TEM foils were cleaned using a Fischione Plasma Cleaner to remove the carbonaceous contamination. Low-magnification loop characterization was performed in a JEOL 3011 TEM operated at 300 keV. A double Cs-corrected JEOL 3100R05 STEM operated at 300 keV was employed for STEM-bright field (STEM-BF) and high angle annular dark field (HAADF) imaging.

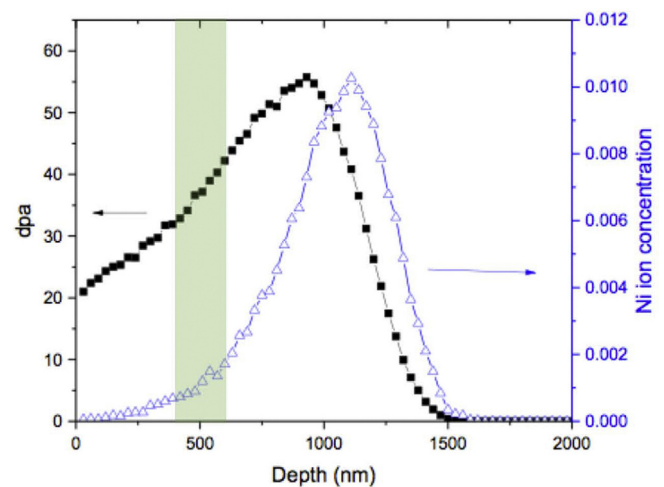


Fig. 1. Depth profiles of displacement per damage (dpa) and induced Ni ion concentration predicted by SRIM code for SP-CSAs irradiated with 3 MeV Ni^{2+} ions to a fluence of 5×10^{16} ions/ cm^2 .

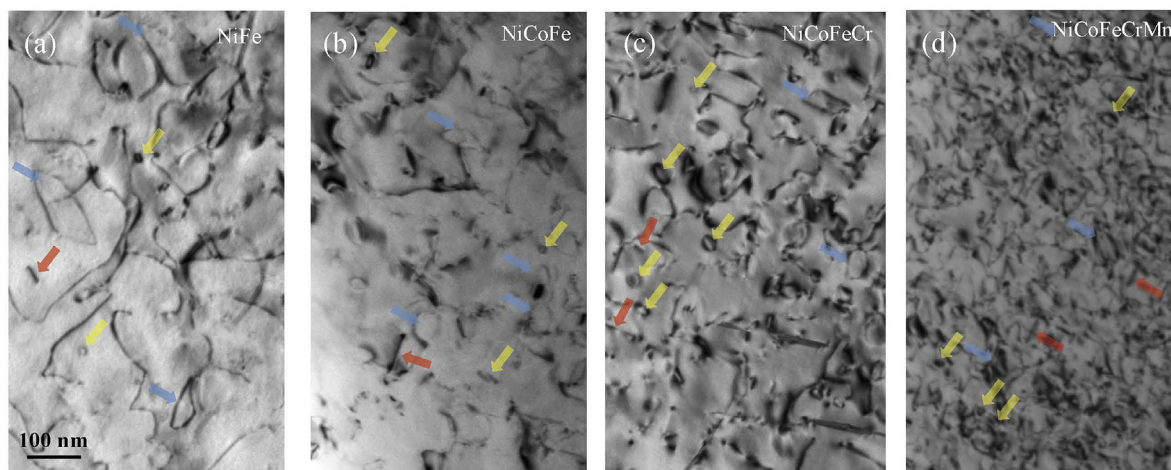


Fig. 2. Dislocation loops in kinetic two-beam condition BF images of SP-CSAs irradiated to 38 ± 5 dpa at 773 K. Perfect loops are marked by blue arrows, faulted loops are marked by yellow arrows, edge-on faulted loops are marked by red arrows. (a) NiFe; (b) NiCoFe; (c) NiCoFeCr; (d) NiCoFeCrMn. (For interpretation of the references to colour in this figure legend, the reader is referred to the web version of this article.)

Local compositional distributions across defect clusters (loops, voids) were analyzed using a Gatan Quantum 965 GIF system with a fast STEM spectrum imaging (STEM SI) system equipped on the JOEL 3100R05. EEL spectra were recorded using a $2k \times 2k$ UltraScan camera. The EELS experiments were performed with a probe size about 0.2 nm and a very small camera length combined with a 9 mm entrance aperture that gives a very large collection angle (>140 mrad). A dispersion of 1 eV/pixel was used and an energy resolution of 2 eV was obtained. The raw intensity data extracted from EELS spectra were all exported into relative composition profiles for quantitative analysis using the Gatan DigitalMicrograph software.

Prior to EELS acquisition, the TEM foils were tilted to an orientation with the electron beam direction parallel to $[110]_{\text{fcc}}$ in order to obtain the edge-on images of dislocation loops on the $\{111\}$ planes. The analysis of edge-on loops can minimize the effect of the surrounding matrix and also maximize the compositional signal from the chemical segregation [14].

2.4. Simulation methodology

Molecular static (MS) modeling was employed in this study. The Fe-Fe, Ni-Ni and Fe-Ni interactions are described by potential EAM-13 developed by Bonny et al., in 2013 [20]. This potential is extensively benchmarked against DFT calculations and previously developed EAM-11 potential [21]. The EAM-13 potential well reproduces the properties of Fe10Ni20Cr alloy [20]. Since this potential predicts a stable fcc phase in the complete concentration range and provides excellent agreement of point-defect solute interaction in the fcc Ni matrix [20], thus, it can be used to calculate the energy state to describe the possible segregation process explored in experiments.

3. Results

3.1. Dislocation loops

Fig. 2 shows BF images of dislocation loops in $[110]$ grains of NiFe, NiCoFe, NiCoFeCr and NiCoFeCrMn after irradiation. All micrographs in Fig. 2 were taken under two-beam kinematical BF conditions using a diffraction vector $g = 200$. After irradiation, the dislocation loops in binary NiFe exhibited the largest size and the

lowest number densities, while those in the HEA NiCoFeCrMn were the smallest and most densely distributed.

The number densities of loops were deduced from more than 10 TEM images from each sample for accuracy with the foil thicknesses measured by EELS. Fig. 3(a) presents the loop number densities in four Ni-containing SP-CSAs after 38 ± 5 dpa irradiation at 773 K. The loop densities in NiCoFe and NiCoFeCr were found to be approximately two times greater than that in NiFe. More importantly, loop number density in HEA NiCoFeCrMn was about one magnitude higher than that in binary NiFe. The loop density may seriously influence the radiation-induced hardening in the materials. More discussion will be followed below.

Fig. 3(b) and (c) demonstrate the size distribution and average diameter of dislocation loops in the four alloys after irradiation. The loop sizes were determined by measuring the longest axis of loops. NiFe shows the largest loop size with an average diameter of 76 nm. To be noted, many larger-sized loops (>150 nm) were observed in the NiFe alloy but not in the rest three alloys. NiCoFe, NiCoFeCr and HEA NiCoFeCrMn have smaller loops than NiFe does, with average diameters of 42 nm, 51 nm and 24 nm, respectively.

The nature of dislocation loops in NiCoFeCr determined by the inside-outside method [22] was presented in Ref. [12]. It is confirmed that, after irradiation at 773 K, the interstitials survived from recombination in NiCoFeCr have clustered into dislocation loops, while the survived vacancies clustered into voids. Similar tests conducted on other alloys also showed that dislocation loops in these Ni-containing alloys are all interstitial type. The loop geometries in the alloys consist of a mixture of perfect $1/2 \langle 110 \rangle$ and faulted $1/3 \langle 111 \rangle$ loops, which are marked in blue and yellow arrows in Fig. 2, respectively. The edge-on images of faulted $1/3 \langle 111 \rangle$ loops were marked by red arrows. Clearly, perfect loops were much larger than the faulted loops in all four alloys. Fig. 3(d) shows the fraction of faulted $1/3 \langle 111 \rangle$ loops in different alloys. The fraction of faulted loops in NiFe is 8%. With increasing composition complexity, the fraction increased to 17%, 34% and 52% in NiCoFe, NiCoFeCr and NiCoFeCrMn, respectively.

3.2. Radiation induced segregation on defect clusters

Segregation on defect clusters, including dislocation loops and vacancies, was characterized using EELS. High resolution STEM micrographs were employed to locate the defect clusters. Fig. 4(a) is

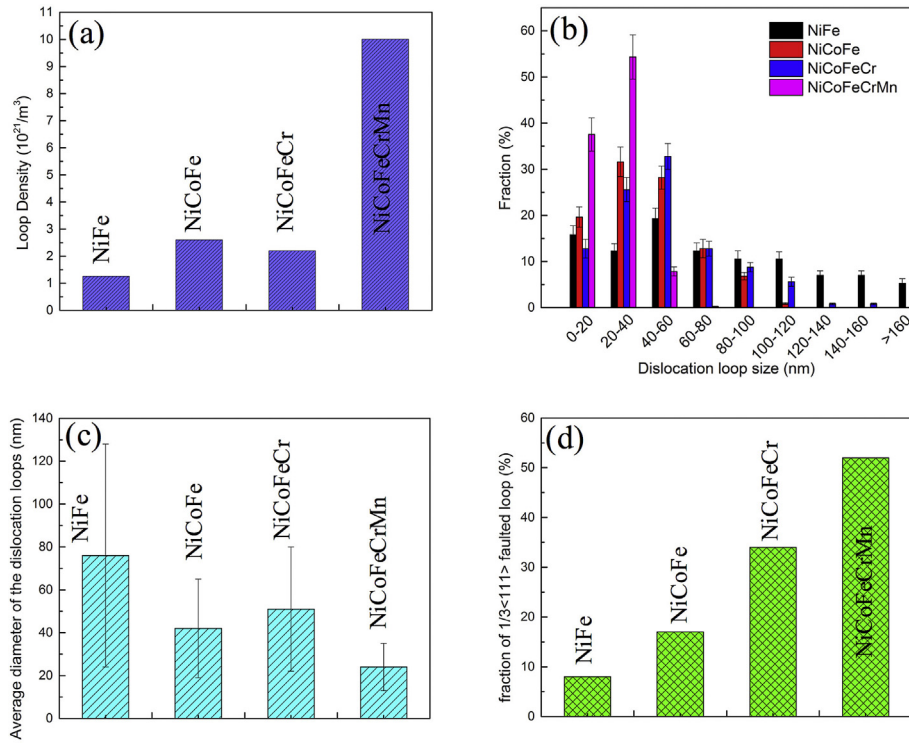


Fig. 3. (a) Loop density; (b) Loop size distribution; (c) Average diameter of loops; (d) Fraction of $1/3\langle 111 \rangle$ faulted loops in SP-CSAs irradiated to 38 ± 5 dpa at 773 K.

a STEM-BF micrograph of an edge-on dislocation loop in irradiated NiCoFeCr. The half atomic plane was marked by “T” sign as shown in Fig. 4(b), indicating that this dislocation loop was an interstitial

type $1/3\langle 111 \rangle$ faulted loop. The faulted loop was in parallel with the incident electron beam. Fast STEM SI was conducted in the selected region marked by white rectangle in Fig. 4(a). A summed

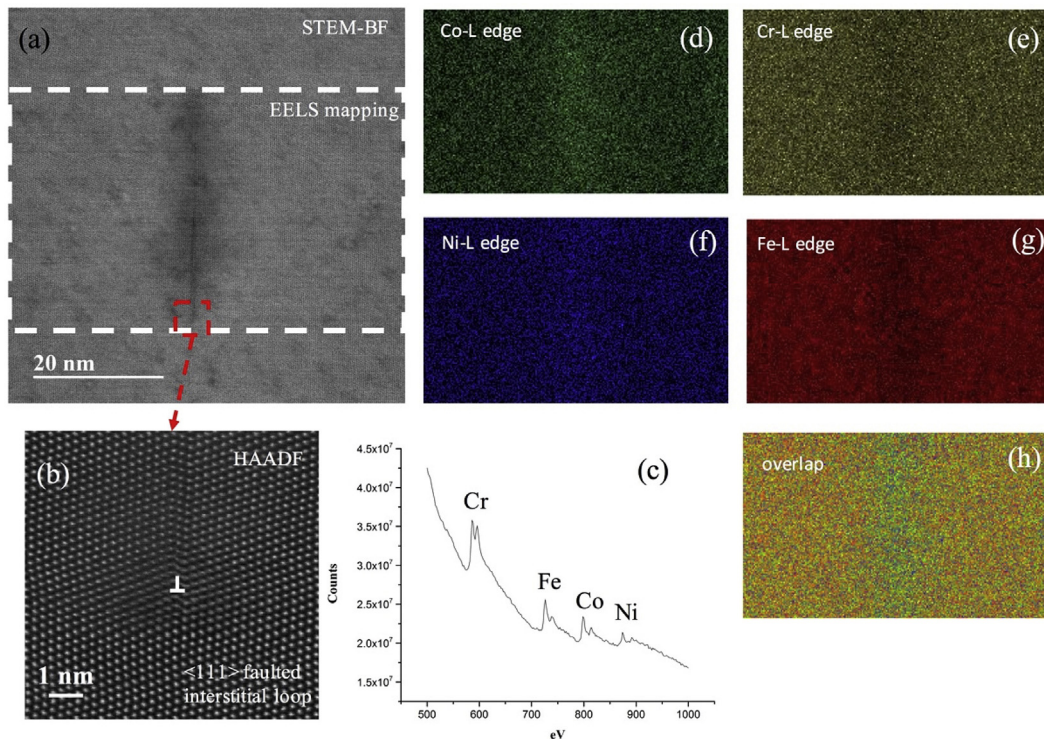


Fig. 4. RIS near a dislocation loop in NiCoFeCr. (a) STEM-BF image of a dislocation loop; (b) high-resolution HAADF image indicates the interstitial type of dislocation loop in (a); (c) EELS spectrum; (d ~ g) EELS mapping results of selected region in (a); (h) overlap image composed by (d ~ g).

EELS spectrum is shown Fig. 4(c) with the peaks, which are all L_{23} peaks, from the different elements labeled. The element distributions around the faulted loop are shown in Fig. 4(d–g), which directly indicate the enrichment of Ni and Co as well as depletion of Fe and Cr around the center of the loop. Fig. 4(e–g) were superimposed in Fig. 4(h) to enhance the visual contrast. RIS on voids was also characterized in this study. Fig. 5(a) shows a HAADF image of irradiated NiCoFeCr. Two voids are shown in dark contrast because of the smaller mass in the area. EELS mapping results in Fig. 5(b–e) show that the inner surface of voids exhibits the same segregation behavior as near faulted loops, with enrichment of Co and Ni, and depletion of Cr and Fe.

RIS behaviors in the other three alloys were all characterized by EELS as well. The composition profiles across the dislocation loops extracted from EELS mapping results are shown in Fig. 6. As mentioned previously, to enhance the detectability of each element, we used an advanced Gatan image filter system attached to a Cs-corrected STEM with a cold-field emission gun. A relatively large probe size and hence a large beam current (about 63 pA) together with a large collection angle (>140 mrad) was used for all the EELS spectra collections. As the studied materials consist of all 3d transition metals with their L_{23} -edge EELS spectra dominated intense sharp peaks a few eV wide, the detection limit for those elements should be at 0.1% level. The visibility of the segregation of the elements can be judged from the obtained curves shown in Fig. 6 using Rose criterion, i.e., a factor 3 was used for judging a peak feature from its background [23]. Clearly, NiFe, NiCoFe and NiCoFeCr showed significant elemental segregation and depletion near the loops. Ni and Co are always enriched while Cr and Fe are always depleted around the defect clusters in these three alloys. The typical full width half maximum (FWHM) extent of the solute segregation region adjacent to the loops in three alloys is about 10 nm. To be noted, HEA NiCoFeCrMn showed no obvious RIS near the loops. This suggests either no segregations or the segregation is too weak to be detected by EELS. It is worth noting that the quantitative analysis of the RIS near loops may be ambitious, because the EELS signal could be affected by the changes of matrix composition and loop sizes. Nevertheless, it is reasonable to deduce a qualitative trend based on current results as shown in Fig. 6. The measured amount of element enrichment or depletion is significantly lower in NiCoFeCrMn than in NiCoFeCr, while it is slightly lower in NiCoFeCr than in NiFe and NiCoFe after high temperature irradiation. Clearly, alloy composition plays a significant role in segregation behavior. Complex compounds may increase the

complexity of RIS process and reduce the RIS level in SP-CSAs.

4. Discussion

4.1. Loop evolution and hardening effect in SP-CSAs

The primary irradiation-induced damages in the structural materials include voids, dislocation loops and local chemical segregation. As a new family of alloys, the studies of SP-CSAs under high temperature irradiation are very limited. Jin et al. found that the swelling behavior of SP-CSAs was strongly controlled by the number and type of alloying elements [7]. The hardening of the alloys after irradiation was also studied, but the detailed mechanisms were not concluded due to the lack of information on dislocation loops [7]. Lu et al. observed both dislocation loops and voids in SP-CSAs by cross-sectional TEM characterization, and explored the intrinsic mechanisms of void resistance in SP-CSAs [12]. However, that previous study mainly focused on the depth distribution of loops and voids, detailed analysis of loop formation and evolution were still scarce [12]. The present work systematically studied the distribution and evolution of dislocation loops in irradiated SP-CSAs and provided much needed information for filling the gap between microstructure changes and mechanical properties of these alloys [7].

Four SP-CSAs presented different stages of formation and growth of faulted loops. It is known that, in fcc structure alloys, the loop growth is through interstitial atom absorption on the $\{111\}$ planes. With increasing doses, faulted loops could transform into unfaulted/perfect loops according to the known reaction [24]:

$$(a/3)\langle 111 \rangle + (a/6)\langle 112 \rangle = (a/2)\langle 110 \rangle \quad (1)$$

The process of faulted/unfaulted loop transformation with increasing irradiation dose has been observed in NiFe. Fig. 7 shows the two-beam condition BF images from binary NiFe alloys irradiated to doses of 0.53 and 4 dpa, respectively. Blue arrows indicate unfaulted loops and yellow arrows indicate faulted loops. The information on average loop diameter, loop density and the fraction of faulted loops is summarized in Table 1. Clearly, with increasing irradiation dose, not only the size of loops increased, the density of the loops decreased, but also the fraction of faulted loops significantly decreased. It is exactly the same loop evolution process based on above growth mechanism. Therefore, on the basis of above observation, we speculate that the loops in NiCoFeCrMn

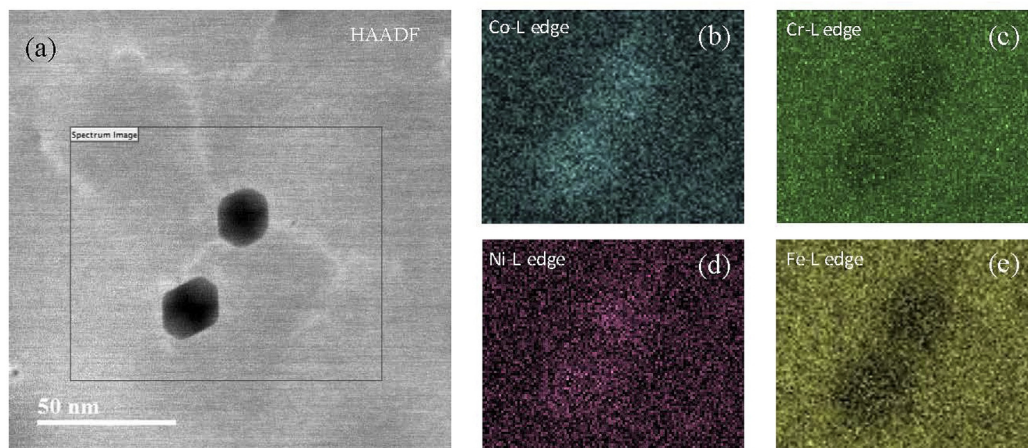


Fig. 5. RIS near the voids in NiCoFeCr. (a) HAADF image of voids; (b – e) EELS mapping results of selected region in (a) indicate Co and Ni enrichment, Cr and Fe depletion near the voids.

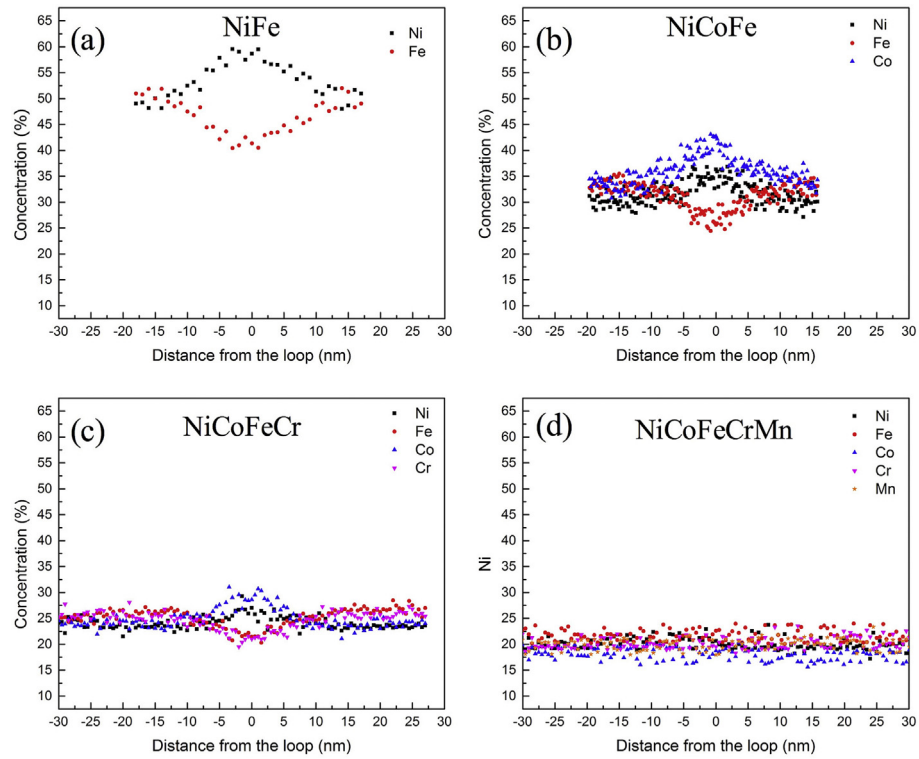


Fig. 6. Composition profiles across the dislocation loops in (a) NiFe; (b) NiCoFe; (c) NiCoFeCr; (d) NiCoFeCrMn.

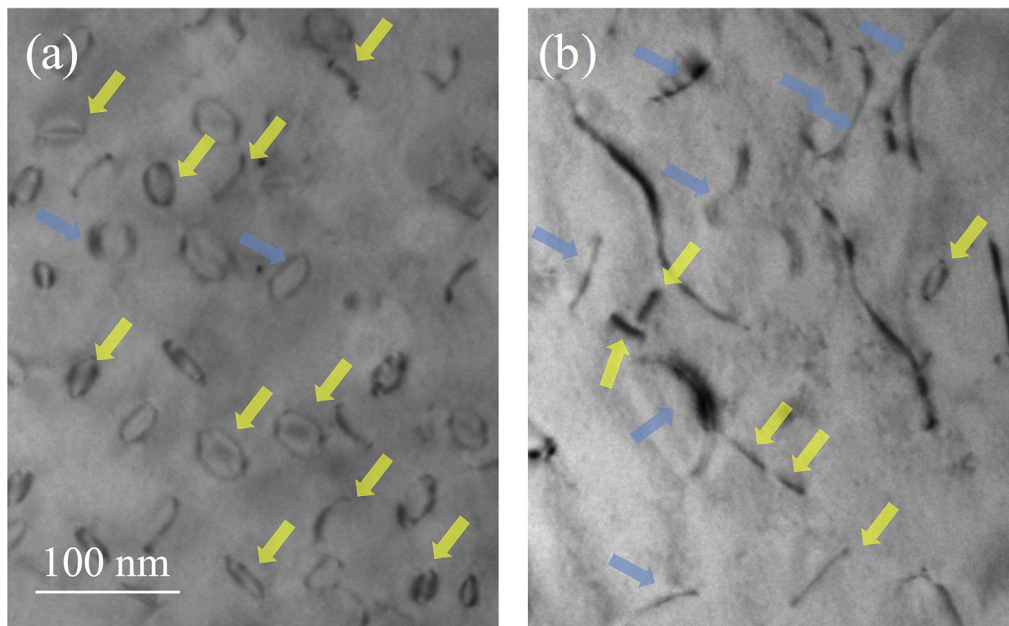


Fig. 7. Dislocation loops in kinetic two-beam condition BF images of NiFe irradiated to (a) 0.53 dpa and (b) 4 dpa at 773 K. Perfect loops are marked by blue arrows, faulted loops are marked by yellow arrows. (For interpretation of the references to colour in this figure legend, the reader is referred to the web version of this article.)

Table 1

Dislocation loop size, density, fraction of faulted loop in NiFe irradiated to 0.53 dpa and 4 dpa at 773 K.

	Dose	Average loop size	Loop density	Fraction of faulted loop
NiFe	0.53 dpa	28 ± 2.2 nm	$(3.5 \pm 0.4) \times 10^{21} \text{ m}^{-3}$	$88 \pm 4.2\%$
	4 dpa	45 ± 4.8 nm	$(1.9 \pm 0.2) \times 10^{21} \text{ m}^{-3}$	$40 \pm 2.8\%$

were in an initial stage of evolution, because NiCoFeCrMn formed smaller size and higher fraction of faulted loops compared to others as shown in Figs. 2 and 3. NiCoFe and NiCoFeCr were likely to be in a medium stage of loop evolution while NiCoFeCr was in an earlier stage than NiCoFe due to the higher density faulted loops. Apparently, the loops in NiFe were in a relatively later stage of evolution among four alloys because faulted loops were mostly transferred into perfect loops and grown into an incredible size. Overall, the analysis of loop behavior in each alloy indicated that the incubation period for faulted to perfect loop transformation was extended in more complex alloys, such as in NiCoFeCrMn and NiCoFeCr. In other words, increasing number of elements and properly adjusting elemental type can delay the loop growth in SP-CSAs. However, since high density sessile dislocation loops in complex alloys may contribute to radiation hardening of the material, the suppression of loop evolution may not be a preferred behavior. Radiation hardening of the studied alloys was measured using nano-indentation [7]. A Nanoindenter XP was utilized for the tests using a Berkovich triangular pyramid indenter. A number of indentations was performed both in the pristine region and irradiation region with a constant $\dot{P}/P = 0.05 \text{ s}^{-1}$. Among the four alloys investigated in the study, NiFe presented the lowest hardening effect and NiCoFeCrMn showed the largest hardening effects. The source of hardening has been speculated to be dislocation loops [21], that is also confirmed in this study. As shown in Fig. 3, binary alloy NiFe with the lowest loop density has the lowest relative hardening between pristine and irradiated region, while HEA NiCoFeCrMn with highest loop density has the strongest relative hardening effect. Radiation hardening of Ni and NiCo as a function of irradiation dose is also reported in Ref. [21]. The result showed that the hardening of Ni increased to 25% with increasing ion fluence up to $1 \times 10^{16} \text{ ions/cm}^2$, but decreased when the ion dose increased further, dropping to ~6% at $5 \times 10^{16} \text{ ions/cm}^2$. The decrease in the hardening effect was attributed to the decreased density of dislocation loops due to the loop growth at high irradiation dose. However, the hardening of NiCo at a fluence of $1.5 \times 10^{16} \text{ ions/cm}^2$ is similar to that at $5 \times 10^{16} \text{ ions/cm}^2$. The result indicates that the evolution of harness in Ni and NiCo was similar, but the process in NiCo was delayed. Therefore, based on the hardening results in Ref. [21] and the microstructure characterizations in this study, we conclude that the hardness change is delayed with increasing compositional complexity in SP-CSAs with slower dislocation loop evolution.

4.2. RIS on dislocation loops

RIS on grain boundaries has been extensively studied in many materials. For instance, it is well known that the radiation induced Cr depletion at grain boundaries in 304L and 316L austenitic stainless steels is considered as the main reason to cause IASCC [13,25]. However, very limited studies have been conducted on RIS behavior of dislocation loops. It is generally believed that the segregation behavior of elements on dislocation loops is similar to that at grain boundary, but at a lower magnitude due to the lighter sink strength [14]. RIS on loops may also affect mechanical properties, because dislocation loops are the preferential sites for the new phase nucleation. If the concentration of the solute near the loop exceeds its solubility limit due to the RIS, a new phase may form.

In this study, we observed the enrichment of Ni and Co, along with the depletion of Cr, Fe and Mn at interstitial type dislocation loops in SP-CSAs (NiFe, NiCoFe, NiCoFeCr and NiCoFeCrMn) with EELS. The results mirrored the RIS behavior at grain boundaries reported in the previous study [9]. Actually, numerous studies have shown that Ni enriches, while Cr and Mn deplete at the grain

boundaries in austenitic stainless steels [13,14,25] and claimed that the observed segregation behavior could be explained by the inverse Kirkendall (1 K) mechanism, which predicts enrichment of fast diffuser, Ni, and depletion of slow diffuser, Cr and Mn, at sinks. Similarly, in this study, although the migration energies of each element in SP-CSAs are still unknown due to the lack of kinetic databases, especially for the complex alloys, we can still explain the enrichment of Ni and Co at the sinks based on the fact that they are faster diffusers, while Fe, Cr and Mn deplete because they are slower diffusers. Detailed kinetic calculations are needed to further understand the segregation behavior in SP-CSAs. The solute size effect seems to be able to perfectly explain the trend of the segregation behaviors of all SP-CSAs observed in this study. Ni and Co as undersized elements tend to diffuse as interstitials to the loops, while Fe, Cr and Mn as oversized elements tend to exchange with vacancies diffusing away from loops. However, since voids are condensed by the vacancies, it is somewhat strange to see that the RIS at voids exhibits the same behavior with that at interstitial loops. Based on the above mentioned mechanism, oversized atoms should be segregated around the voids because of their association with vacancy flux. The reason behind this unexpected result needs further investigation.

The final observed microstructures are the integrated results of defect production, recombination, migration and clustering. The suppression of RIS behavior in NiCoFeCr and NiCoFeCrMn indicates that increasing the elemental complexity has a significant impact on defect evolution in SP-CSAs. Atoms of different elements sit randomly among the lattice sites in SP-CSAs. This may introduce the large disturbance of the lattice structure. Our recent studies have concluded that compositional complexity has significant influence on the irradiation response in materials [5,8], which give us a reasonable explanation on the reduced RIS level in NiCoFeCr and NiCoFeCrMn: high lattice distortion may significantly slug the defect diffusion and enhance the vacancy/interstitial recombination, reduce the flux of defects toward the sinks, and sequentially increase the complexity of RIS process and suppress RIS level in more complex alloys.

4.3. Segregation region close to a dislocation loop revealed by modeling

EELS characterization has been conducted on some non-edge-on faulted loops, but it is unable to observe any RIS because of low signals. In order to clarify the style of segregation region around a $1/3\langle 111 \rangle$ faulted dislocation loop, computational simulations have been performed to determine the energy landscape of different segregation states. A disk or a ring shape of the dislocation model is considered. A $1/3\langle 111 \rangle$ dislocation loop with a radius (R) of 2.5 nm was constructed by inserting one extra atomic layer along the $\langle 111 \rangle$ direction. The stress field introduced by the insertion was firstly relaxed by moving the related atoms according to the calculated displacements. The computational box was built with X, Y and Z along the $[111]$, $[1\bar{1}2]$ and $[\bar{1}10]$ directions, respectively, and the length along each direction is around 10 nm. The molecular static (MS) method was used to relax the system at 0 K and calculate the total energy without considering entropy effect. After relaxation, the core of a loop was identified within the region of $R \pm \Delta R$, as shown in Fig. 8. Here, ΔR was set to be 0.5 nm and 1.0 nm for comparison. Two cases were tested for identifying the segregation region.

Case I (local segregation): The calculation mainly focused on the local region around a faulted loop, where the total number of atoms within the region of $R \pm \Delta R$ has been considered. In this case, the concentration of Fe around the loop was set to be 0.4, which is smaller than 0.5 of HEA. Four models were considered (Fig. 9).

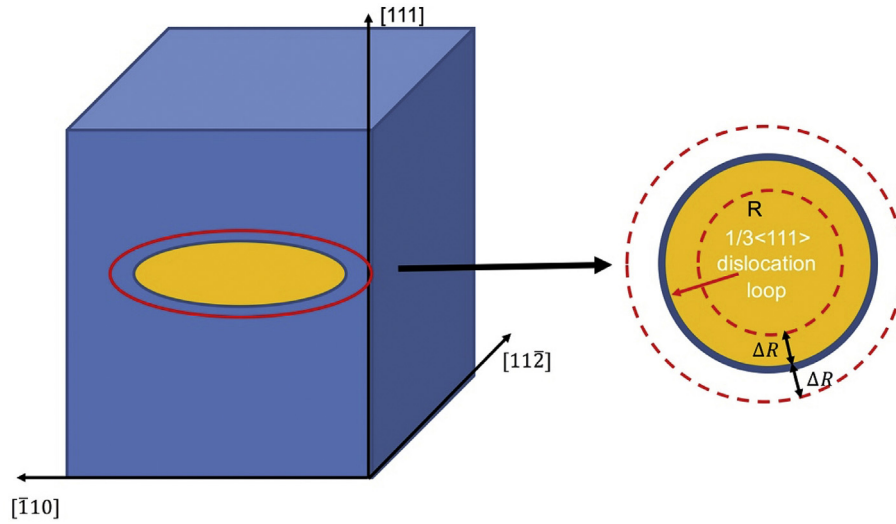


Fig. 8. Schematic illustration of the settings of $1/3\langle 111 \rangle$ dislocation loop in fcc matrix for MS simulation.

- (1) Both Fe and Ni atoms are uniformly distributed in the whole region (Disk);
- (2) Fe atoms are distributed in the region defined by $R-\Delta R$, and thus the core region of the loop is occupied by Ni atoms (Ring-1);
- (3) Fe atoms are partially distributed in both the region defined by $R-\Delta R/2$ and the region defined from $R+\Delta R/2$ to $R+\Delta R$ (Ring-2);
- (4) Fe atoms are distributed around the core region defined from $R-\Delta R$ to $R+\Delta R$, while Ni atoms are distributed in other regions; thus, the depletion of Fe and the enrichment of Ni around the loop can also be tested, as compared with the models above (Mix).

The total energies of the four segregation models are shown in Fig. 10(a), but only with $\Delta R = 0.5$ nm because the energy trends for ΔR values of 0.5 nm and 1.0 nm are the same. The “disk” like configuration has the lowest total energy. The total energy of both ring-1 and ring-2 is higher than the “disk” like configuration. Comparing to the atomic configurations of “disk” like, ring-1 and ring-2, mix type has the highest concentration of Fe. From Fig. 10(a), it is also clear that the enrichment of Fe around the loop core significantly increases its energy, indicating that the depletion of Fe is preferred around a faulted loop.

Case II (global segregation): The above model focused on the local region around the dislocation loop. In order to understand the global effect on segregation, the distributions of Fe and Ni atoms in

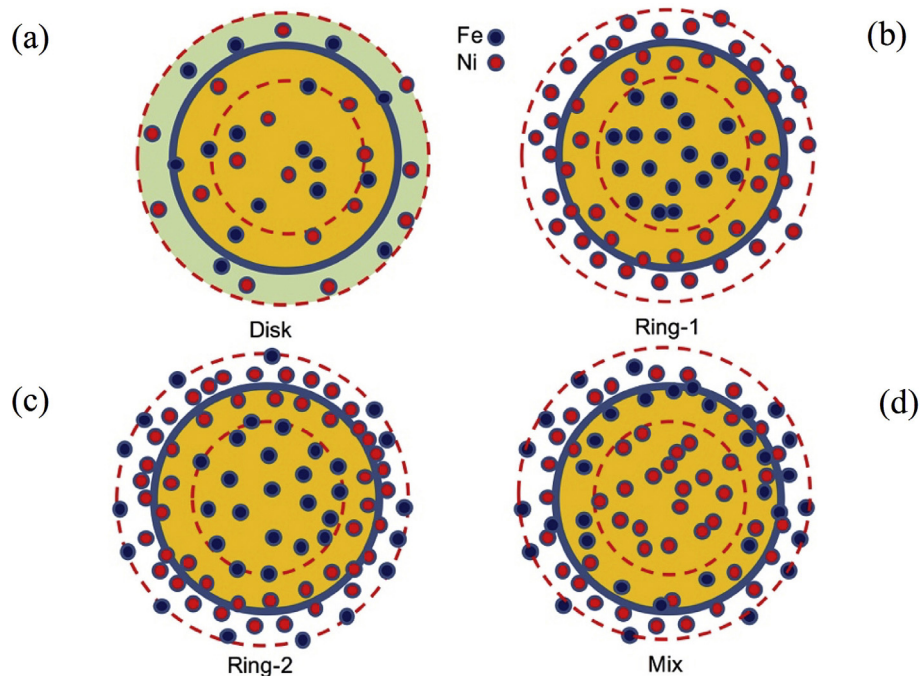


Fig. 9. Four segregation models near a $1/3\langle 111 \rangle$ loop in NiFe. (a) “disk” like; (b) Ring-1; (c) Ring-2; (d) Mix.

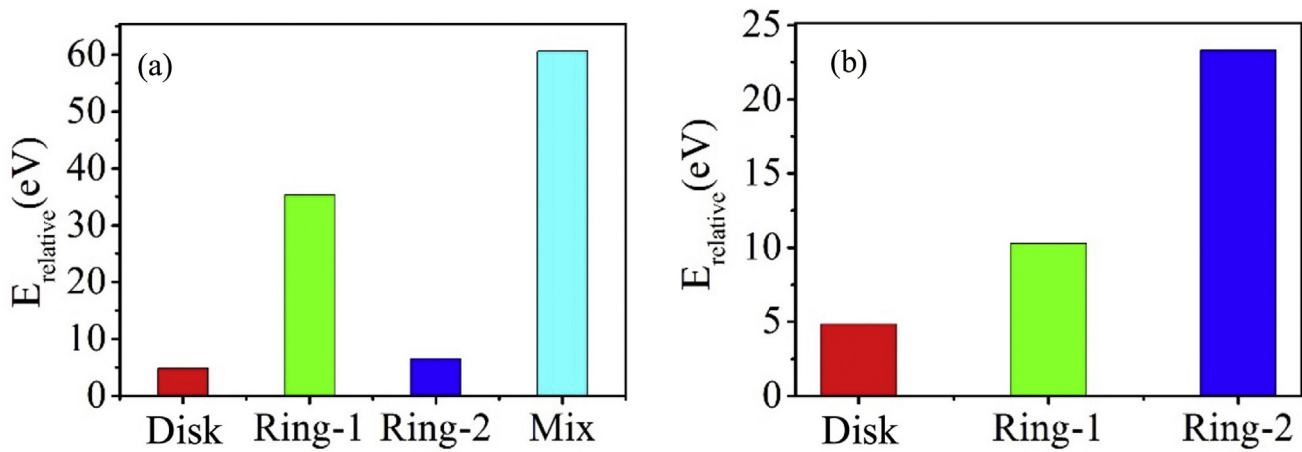


Fig. 10. The calculated total energy for four segregation models (a) local segregation; (b) global segregation.

the whole computational box were also considered. Three models were employed for this case:

- (1) Ni and Fe atoms are uniformly distributed with an equal molar concentration, even in the core of a $1/3\langle 111 \rangle$ dislocation loop. The radius of this loop is also set to be 2.5 nm and the core region is defined again by $R \pm \Delta R$ with $\Delta R = 0.5$ nm. Based on this assumption, the number of Ni and Fe atoms in the core region is defined as N_{Ni} and N_{Fe} (Disk);
- (2) Based on above model, we increase N_{Ni} to $1.5 N_{Ni}$ and decrease N_{Fe} to $N_{Fe} - 0.5 N_{Ni}$. However, the $0.5 N_{Fe}$ atoms are inserted to the matrix to replace Ni atoms, thus increasing Fe concentration in the matrix, but the concentration of Ni and Fe in the system is still equal (Ring-1);
- (3) We continue to increase the number of Ni atoms and set all the atoms in the core region of the dislocation to be Ni atoms. The Fe concentration in the matrix increases by replacing Ni atoms with N_{Fe} Fe atoms. However, the concentration of Ni and Fe in the system is equal (Ring-2).

The calculated energies for these models are shown in Fig. 10(b). Again, the “disk” like configuration has the lowest energy state. Therefore, both the local and global calculations suggest that the segregation region prefers a “disk” like configuration, rather than

ring type configurations for a binary NiFe system under radiation. Although MS simulations have not been conducted on other SP-CSAs alloys, it is reasonable to assume that “disk” like segregation will be also preferred at the periphery of faulted loops, because SP-CSAs exhibit a similar RIS behavior as we discussed above. One of the possible reasons for the preference of a “disk” like segregation may be associated with the uniform distribution of stress field of a faulted loop. Fig. 11 shows the schematic of the stress fields of faulted (a) and perfect (b) loops. For a faulted loop, the high stress field appears not only around the core region, but also through the whole loop because of atomic stacking. For a perfect loop, the high stress field appears only around the core region, although the lower stress field also exists through the whole loop, which may occur from the possible mixture of Ni and Fe atoms. Therefore, the high stress field introduced from the stacking fault may be one of the reasons for the “disk” like segregation. Hence, for perfect dislocation loops, the ring type configurations would be preferred. Further calculations are needed to clarify such a hypothesis.

This study presents three different aspects of radiation response that are related to RIS in SP-CSAs, i.e., dislocation loop evolution, RIS behavior and loop configurations. The observed phenomenon can all be attributed to the sluggish diffusion of the atoms in more chemically complex SP-CSA alloys. Generally speaking, with increasing compositional complexity, the loop evolution has been

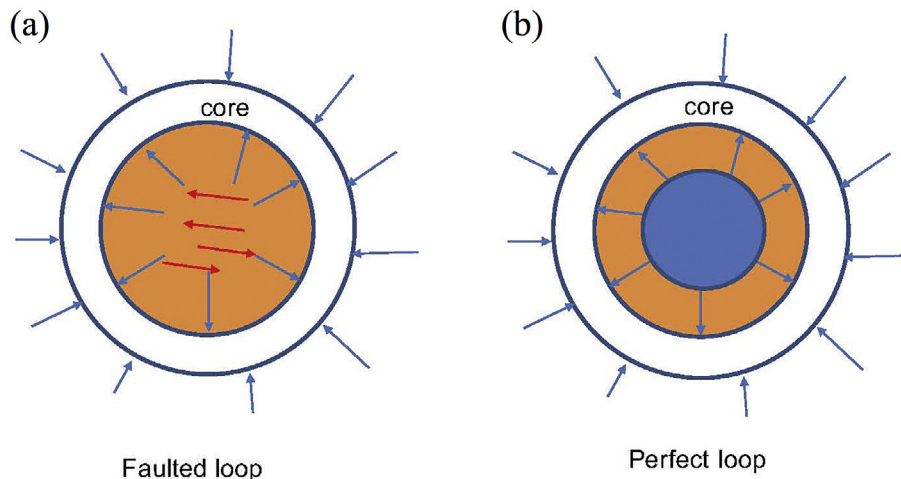


Fig. 11. Schematics of stress field around (a) a faulted loop; (b) a perfect loop.

significantly delayed due to the slower atom diffusion, resulting in high density of small faulted loops. The higher density of loops can further disperse the flux of defects toward the sinks, causing the weak RIS behavior in more complex alloys. Weak RIS can inhibit the formation of new phase and stabilize the chemical complexity of the matrix. On the other hand, the “ring” like segregation with relatively larger scale is preferred in simpler alloys because of the higher proportion of large perfect loops, while the “disk” like segregation with smaller scale is preferred in chemically more complex alloys because of the higher density of faulted loops.

5. Conclusion

In summary, an experimental study was conducted on dislocation loop evolution and RIS behavior in a group of four SP-CSAs with increasing chemical complexity. The samples were irradiated by Ni^{2+} ions at 773 K to a fluence of 5×10^{16} ions/cm². Both perfect $1/2\langle 110 \rangle$ and faulted $1/3\langle 111 \rangle$ interstitial dislocation loops were observed in all studied alloys. The fraction of $1/3\langle 111 \rangle$ faulted loops increased with increasing complexity of compositions in SP-CSAs. Increasing compositional complexity extended the incubation period and delayed the loop growth. RIS behavior in SP-CSAs was also studied and the results can be summarized as Ni and Co enrich, but Cr, Fe and Mn deplete near defect clusters (dislocation loops and voids). RIS phenomenon has been significantly reduced by increasing composition complexity, such as in NiCoFeCr and NiCoFeCrMn. High lattice distortion in more complex alloys suppresses RIS due to the reduced interstitial migration. According to the MS simulation, “disk” like segregation is preferred to form near the faulted dislocation loops in SP-CSAs.

Acknowledgments

This work was supported as part of the Energy Dissipation to Defect Evolution (EDDE) Center, an Energy Frontier Research Center funded by the US Department of Energy, Office of Science, Basic Energy Sciences. Ion beam work was performed at the UT–ORNL Ion Beam Materials Laboratory located on the campus of the University of Tennessee–Knoxville. Microstructure characterizations were conducted in the Michigan Center for Material Characterization of the University of Michigan.

References

- [1] B. Gludovatz, A. Hohenwarter, D. Catoor, E.H. Chang, E.P. George, R.O. Ritchie, A fracture-resistant high-entropy alloy for cryogenic applications, *Science* 345 (2014) 1153–1158.
- [2] L.J. Santodonato, Y. Zhang, M. Feygensohn, C.M. Parish, M.C. Gao, R.J.K. Weber, J.C. Neufeld, Z. Tang, P.K. Liaw, Deviation from high-entropy configurations in the atomic distributions of a multi-principal-element alloy, *Nat. Commun.* 6 (2015) 5964, <http://dx.doi.org/10.1038/ncomms6964>.
- [3] K.G. Pradeep, Y. Deng, Z. Li, D. Raabe, C.C. Tasan, Metastable high-entropy dual-phase alloys overcome the strength–ductility trade-off, *Nature* (2016) 1–8, <http://dx.doi.org/10.1038/nature17981>.
- [4] F. Otto, Y. Yang, H. Bei, E.P. George, Relative effects of enthalpy and entropy on the phase stability of equiatomic high-entropy alloys, *Acta Mater* 61 (2013) 2628–2638.
- [5] Y. Zhang, G.M. Stocks, K. Jin, C. Lu, H. Bei, B.C. Sales, L.W. Wang, L.K. Beland, R.E. Stoller, G.D. German, M. Caro, A. Caro, W.J. Weber, Influence of chemical disorder on energy dissipation and defect evolution in concentrated solid solution alloys, *Nat. Commun.* 6 (2015) 8736, <http://dx.doi.org/10.1038/ncomms9736>.
- [6] C. Lu, K. Jin, L.K. Beland, F. Zhang, T. Yang, L. Qiao, Y. Zhang, H. Bei, H.M. Christen, R.E. Stoller, L.M. Wang, Direct observation of defect range and evolution in ion-irradiated single crystalline Ni and Ni binary alloys, *Sci. Rep.* (2016) 1–10, <http://dx.doi.org/10.1038/srep19994>.
- [7] K. Jin, C. Lu, L.M. Wang, J. Qu, W.J. Weber, Y. Zhang, H. Bei, Effects of compositional complexity on the ion-irradiation induced swelling and hardening in Ni-containing equiatomic alloys, *Scr. Mater* 119 (2016) 65–70, <http://dx.doi.org/10.1016/j.scriptamat.2016.03.030>.
- [8] F. Granberg, K. Nordlund, M.W. Ullah, K. Jin, C. Lu, H. Bei, L.W. Wang, F. Djurabekova, W.J. Weber, Y. Zhang, Mechanism of radiation damage reduction in equiatomic multicomponent single phase alloys, *Phys. Rev. Lett.* 116 (2016) 135504–135509, <http://dx.doi.org/10.1103/PhysRevLett.116.135504>.
- [9] N.A.P.K. Kumar, C. Li, K.J. Leonard, H. Bei, S.J. Zinkle, Microstructural stability and mechanical behavior of FeNiMnCr high entropy alloy under ion irradiation, *Acta Mater* 113 (2016) 230–244, <http://dx.doi.org/10.1016/j.actamat.2016.05.007>.
- [10] D.S. Aidhy, C. Lu, K. Jin, H. Bei, Y. Zhang, L. Wang, W.J. Weber, Point defect evolution in Ni, NiFe and NiCr alloys from atomistic simulations and irradiation experiments, *Acta Mater* 99 (2015) 69–76, <http://dx.doi.org/10.1016/j.actamat.2015.08.007>.
- [11] K. Jin, H. Bei, Y. Zhang, Ion irradiation induced defect evolution in Ni and Ni-based FCC equiatomic binary alloys, *J. Nucl. Mater* 471 (2016) 193–199, <http://dx.doi.org/10.1016/j.jnucmat.2015.09.009>.
- [12] C. Lu, L. Niu, N. Chen, K. Jin, T. Yang, P. Xiu, Y. Zhang, F. Gao, H. Bei, S. Shi, M. He, I.M. Robertson, W.J. Weber, L. Wang, Enhancing radiation tolerance by controlling defect mobility and migration pathways in multicomponent single-phase alloys, *Nat. Commun.* 7 (2016) 13564, <http://dx.doi.org/10.1038/ncomms13564>.
- [13] C.M. Barr, G.A. Vetterick, K.A. Unocic, K. Hattar, X.-M. Bai, M.L. Taheri, Anisotropic radiation-induced segregation in 316L austenitic stainless steel with grain boundary character, *Acta Mater* 67 (2014) 145–155, <http://dx.doi.org/10.1016/j.actamat.2013.11.060>.
- [14] Z. Jiao, G.S. Was, Novel features of radiation-induced segregation and radiation-induced precipitation in austenitic stainless steels, *Acta Mater* 59 (2011) 1220–1238, <http://dx.doi.org/10.1016/j.actamat.2010.10.055>.
- [15] T.R. Allen, J.I. Cole, J. Gan, G.S. Was, R. Dropek, E.A. Kenik, Swelling and radiation-induced segregation in austenitic alloys, *J. Nucl. Mater* 342 (2005) 90–100, <http://dx.doi.org/10.1016/j.jnucmat.2005.02.008>.
- [16] Z. Lu, R.G. Faulkner, G. Was, B.D. Wirth, Irradiation-induced grain boundary chromium microchemistry in high alloy ferritic steels, *Scr. Mater* 58 (2008) 878–881, <http://dx.doi.org/10.1016/j.scriptamat.2008.01.004>.
- [17] J.M. Cookson, G.S. Was, P.L. Andresen, Crack Initiation Mechanisms in IASCC of Stainless Steel Alloys, 1995.
- [18] Y. Dong, B.H. Sencer, F.A. Garner, E.A. Marquis, Microchemical and microstructural evolution of AISI 304 stainless steel irradiated in EBR-II at PWR-relevant dpa rates, *J. Nucl. Mater* 467 (2015) 692–702, <http://dx.doi.org/10.1016/j.jnucmat.2015.10.041>.
- [19] R.E. Stoller, M.B. Toloczko, G.S. Was, A.G. Certain, S. Dwaraknath, F.A. Garner, On the use of SRIM for computing radiation damage exposure, *Nucl. Instrum. Methods Phys. Res. B* 310 (2013) 75–80, <http://dx.doi.org/10.1016/j.nimb.2013.05.008>.
- [20] G. Bonny, N. Castin, D. Terentyev, Interatomic potential for studying ageing under irradiation in stainless steels: the FeNiCr model alloy, *Model. Simul. Mater. Model. Simul. Mater. Sci. Eng.* 21 (2013) 085004.
- [21] G. Bonny, D. Terentyev, R.C. Pasianot, S. Poncé, A. Bakaev, Interatomic potential to study plasticity in stainless steels: the FeNiCr model alloy, *Model. Simul. Mater. Sci. Eng.* 19 (2011) 085008–085016, <http://dx.doi.org/10.1088/0965-0393/19/8/085008>.
- [22] M.L. Jenkins, M.A. Kirk, Characterisation of Radiation Damage by Transmission Electron Microscopy, 2000.
- [23] A. Rose, Television pickup tubes and the problem of vision, *Adv. Electr.* 1 (1948) 131–166.
- [24] I.M. Neklyudov, V.N. Voyevodin, Features of structure-phase transformations and segregation processes under irradiation of austenitic and ferritic-martensitic steels, *J. Nucl. Mater* 212 (1994) 39–44.
- [25] G.S. Was, J.P. Wharry, B. Frisbie, B.D. Wirth, D. Morgan, J.D. Tucker, T.R. Allen, Assessment of radiation-induced segregation mechanisms in austenitic and ferritic-martensitic alloys, *J. Nucl. Mater* 411 (2011) 41–50, <http://dx.doi.org/10.1016/j.jnucmat.2011.01.031>.